

Effect of front surface engineering on high energy electron, X-ray and heavy ion generation from Relativistic laser interaction with thick high-Z targets

J. Twardowski,^{1, a)} C. Kuz,² A. S. Bogale,^{3,4} Z. Su,¹ A. Lee,² R. Kaur,¹ M. Eder,² Y. Noor,¹ D. P. Broughton,³ Md Kazi Rokunuzzaman,¹ R. Hollinger,⁵ A. Blackston,¹ J. Strehlow,³ A. Baraona,² P. Spingola,² G. Tiscareno,² D. Hanggi,² B. Unzicker,² C.-S. Wong,³ G. K. Ngirmang,⁶ F. N. Beg,⁴ D. Schumacher,² and E. Chowdhury^{1,7,2}

¹⁾*Department of Materials Science and Engineering, The Ohio State University, Columbus, OH 43210, USA.*

²⁾*Department of Physics, The Ohio State University, Columbus, OH 43210, USA.*

³⁾*Los Alamos National Laboratory, Los Alamos, NM 87545, USA.*

⁴⁾*Center for Energy Research, University of California San Diego, La Jolla, CA 92093, USA.*

⁵⁾*Electrical and Computer Engineering Dept, Colorado State University, Fort Collins, CO 80523, USA.*

⁶⁾*National Sciences and Science Education, National Institute of Education, Nanyang Technological University, Singapore 637616, Singapore.*

⁷⁾*Department of Electrical and Computer Engineering, The Ohio State University, Columbus, OH 43210, USA.*

(Dated: 10 March 2026)

Relativistic lasers on solid targets generate hot electrons, and other secondary particles. These particles can be used for radiography, cancer therapy, or isochoric heating. A lower density or structured coating on high-Z targets can improve laser-target energy coupling and subsequently enhance overall particle emission. In this work performed at the Scarlet Facility, a 10^{21} W/cm² intense pulse was incident on front surface coatings on 1 mm thick Ta. These coatings include a 12 μ m plastic coating, a 50 μ m thick foam coating, and a Au nanowire (NW) coating. Post-damage craters are correlated with reflected light on a MACOR screen, illustrating that less absorption in a target is directly tied to smaller craters. Additionally, more absorption in a target also leads to more MeV electrons and X-rays. Bare targets performed the best for electron and MeV X-ray generation, with X-rays of 30 MeV detected, as coatings tested were too thick and thus experienced lower intensities. Due to this larger spot size, foam and NW-coated targets generated the greatest heavy ion acceleration. Particle-in-cell simulations tested on bare and plastic-coated targets illustrate that $\sim\mu$ m thick plastic coatings perform better than bare Ta. These results underline the importance of density and thickness control of coatings on high-Z materials. In the future, post-damage crater analysis could provide an easy way to benchmark absorption in a sample, and could later be compared against absorption estimates from particle-in-cell simulations.

I. INTRODUCTION

A high intensity laser ($>10^{18}$ W/cm²) incident on a solid target may accelerate electrons relativistically^{1,2}, primarily through $j \times B$ acceleration^{3,4}. These energetic electrons can then seed secondary particles such as: ions⁵, protons⁶, positrons⁷, or MeV X-rays^{8,9}. Ion beams can be used for isochoric heating¹⁰, cancer therapy^{11,12}, radiography¹³, and neutron generation¹⁴. Protons have been used successfully for radiotherapy of specific cancers¹⁵. Meanwhile, X-rays have been utilized in nuclear physics, medicine, radiation effects, or flash radiography^{16,17}. In particular, X-rays generated from high-Z targets have been used for radiography as an alternative to traditional X-ray sources. Bremsstrahlung X-ray sources driven by short pulse lasers have a spot size of ~ 100 μ m, tunable angular distribution, ultrashort duration, and can range up to MeV levels^{1,17,18}. Radiographs taken with a smaller spot size have higher resolution than conventional

sources, where spot size is \sim mm¹. Additionally, these energetic X-rays may be used to radiograph high density objects such as double-shell ignition targets¹⁸, which cannot be penetrated by lower energy sources.

Traditionally, lasers on bare, solid targets can be plagued by low laser-target energy coupling. The main pulse is typically preceded by a prepulse, which when incident on the target ionizes the surface, thus creating an expanding plasma that follows a decaying exponential. As the main pulse propagates through the plasma it encounters an overdense plasma ($\omega_p > \omega_l$) from which the laser pulse is reflected¹⁹. At high intensities it is possible to increase laser-target coupling through relativistic transparency, where relativistic electrons on the sample have increased mass and render a plasma underdense, but it requires high temporal contrast and specific target geometry^{10,19}. However, for bare targets with high intensity lasers, the target may only absorb up to 10% of the laser's energy^{20,21} due to an overdense plasma being reached more quickly thus limiting absorption to a thin surface layer²².

A coating may be used as the front layer of a high-Z target to thus improve laser-target coupling. A coating of nanowires (NWs) or low density aerogels can be used to increase the coupling to 79 - 88%^{21,23}. In these structured targets, more

^{a)} Author to whom correspondence should be addressed: twardowski.justin@gmail.com

electrons can be accelerated into the high-Z substrate before the plasma optically shuts the peak of the pulse²⁴. A thin, solid-density plastic coating can also be used to increase laser absorption into the target, by creating a homogeneous plasma for the laser to interact with^{2,17}. Generally, a solid plastic coating may be more appealing than structured coatings, as structured coatings have more parameters that need to be optimized (such as nanowire length, diameter, density, or a foam thickness and density)^{6,21}, and are less costly to produce.

In this work conducted at the Scarlet Facility, a 815 nm, 50 fs, 5-7 J pulse was incident on 1 mm thick Ta. Plastic, aerogel/foam, and NW coatings were all tested against bare Ta. Peak intensities on target ranged from $0.5-4 \times 10^{21}$ W/cm², with pre-pulse contrast of 10^{-8} at -75 ps and 10^{-6} at -25 ps. Generated electrons, Ta ions, and MeV X-rays were recorded and characterized simultaneously for each individual target type. In addition, qualitative laser-target coupling efficiency can be described by use of a diffuse reflector (MACOR). Post-damage crater measurements are compared against MACOR images and can offer insight into laser-target energy coupling.

MeV X-rays have not been characterized before at this facility, and both the high contrast and short pulse duration are unusual in these hard X-ray experiments^{8,10}. Nanostructured-coatings are rarely used in these high-Z targets, and more insight into their behavior could prove fruitful for future studies^{2,25}. High laser contrast is crucial with structured targets, as a low-intensity pre-pulse could generate a critical density surface before the arrival of the peak of the pulse²⁶. These results will continue to fill in gaps in the collective understanding about relativistic laser-matter interactions and its subsequent emissions.

II. EXPERIMENTAL SETUP

At the Scarlet Facility (LasernetUS experiment K-10019), a *p*-polarized, 815 nm, 50 fs, 5-7 J pulse was incident at 28° on 1 mm thick bare and coated Ta targets. With an *f*/2 OAP, the focal spot had a $1/e^2$ diameter of 4.2 μm. Peak intensities on target were from $0.5-4 \times 10^{21}$ W/cm², with pre-pulse contrast of 10^{-6} at -25 ps. The experimental setup is shown in Fig. 1(a), while the contrast of the laser is featured in Fig. 2. All targets tested were on a 1 mm thick Ta substrate, with the laser focused on the Ta substrate. Coatings tested were: 12 μm thick photoresist (AZ nLOF2070) with 1.07 g/cc (spin-coated at 500 RPM, from Ohio State University (OSU)), 50 μm thick aerogel (GA-CH) with 15.4 mg/cc (from General Atomics), Au nanowires (NWs) aligned vertically with a diameter of 0.51 ± 0.06 μm and a length of 4.39 ± 0.50 μm (from Colorado State University (CSU)), alongside bare Ta. SEM images of the foam and NW-coated targets are featured in the supplementary materials, Fig. s1. Each different target type was mounted on a rotating wheel that held six targets, so all of the generated electron spectra, X-ray spectra, and ion histograms were cumulative for all six shots. By using this sample holder and a mechanized stage, it was possible to shoot all six targets in one vacuum pump cycle, and the image plates and CR-39 were collected after each set of shots. Target

alignment was performed on the front side of the target, using a microscope objective that was moved out with a mechanized stage during system shots.

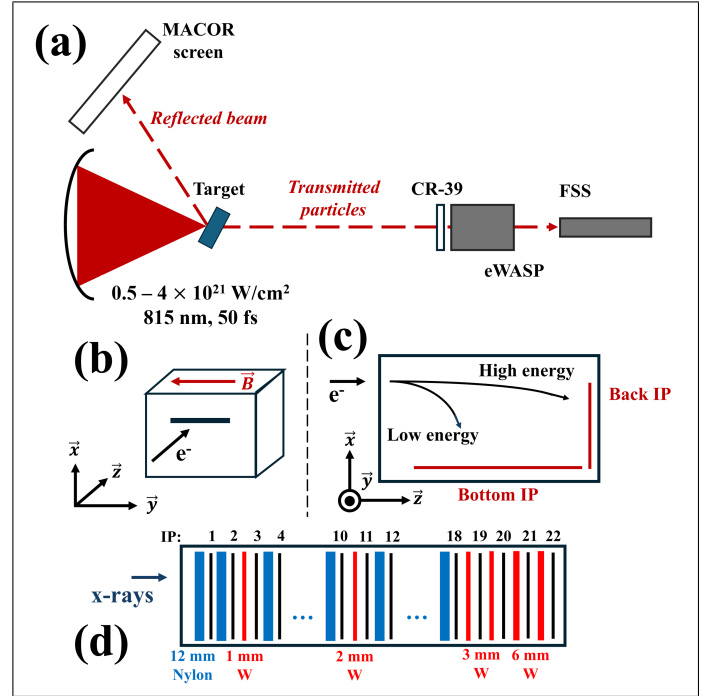


FIG. 1. (a) Experimental setup with an angle of incidence of 28°. The MACOR screen is rotated 50°, and was placed directly next to the focusing optic. The CR-39 is placed behind the target in the laser axis, with a horizontal slit cut out for the electron wide angle spectrometer (eWASP). The filter stack spectrometer (FSS) is placed outside of the chamber and in the laser axis. (b) Front view of 5.1 × 5.1 cm CR-39, and its mylar coating thickness. (c) Side view of eWASP, where the electrons enter the slit in $+\vec{z}$, \vec{B} is in $-\vec{y}$. (d) Side view of FSS, with the IP numbers labeled above the FSS. The majority of the filters are nylon-66, while some are tungsten (W).

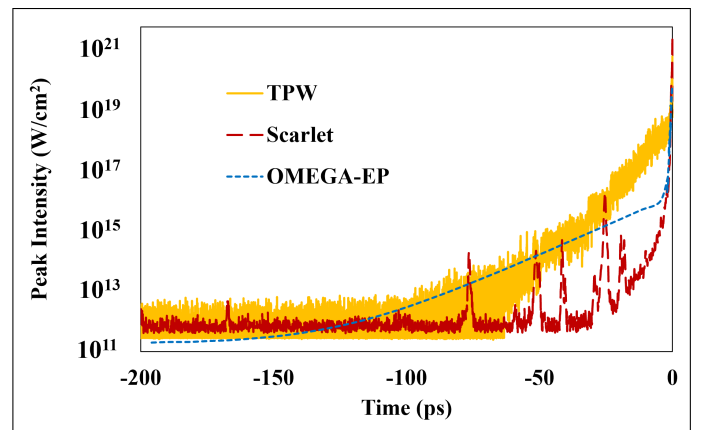


FIG. 2. Measured pre-pulse contrast of Scarlet (cross correlation) versus other high power lasers, with the peak of the pulse occurring at 0 ps.

Behind the target in the laser axis is mylar-coated CR-39.

The mylar is laid in a stepwise fashion over the front, ranging in thickness from 0 - 12 μm which can then discern Ta ions from 0 - 60 MeV (Fig. 1(b)). Protons are visible on etched CR-39, but various energy levels cannot be discerned. The CR-39 has a horizontal slit cut out, 2.5 \times 26 mm, allowing electrons to pass through to the electron wide angle spectrometer (eWASP). The slit was cut out of the CR-39, but mylar was intact over the slit. After being exposed, the mylar was removed and the CR-39 is put in 6 M NaOH at 95 $^\circ$ C for 90 minutes. Afterwards, the CR-39 is put in 100% glacial acetic acid for 90 seconds. Imaging was carried out under an optical microscope at 10x magnification. Ion counts were measured at high resolution for the entire sample from a stitched-together image (via homemade machine-learning Python script).

The eWASP is home-built from 316 stainless steel while the sides are mild steel. The front plate is 2.5 cm thick, while the slit is 0.5 mm in width, and 25 mm across. Modeling of the electron trajectories was carried out in Python, and a MPT-132-7s hall probe was used to measure the magnetic field inside the eWASP. The B field deflects the electrons downward ($-\vec{x}$ in Fig. 1(c)) where their final position is determined by their initial energy. The distance between the magnets is 37 cm, leading to a peak magnetic field in the center of the eWASP of 0.35 T. Image plates²⁷ (IPs, BAS-IP SR) were placed at the bottom of the detector, and in the back, while no steel back plate was used (Fig. 1(C)). The eWASP can detect electrons from 1 - 50 MeV.

The filter stack spectrometer (FSS) is behind the eWASP and outside of the target chamber. The FSS is machined out of tungsten, and carries a stack of alternating filters and image plates. X-rays are attenuated by the filters and deposit their energy on the IPs, building a diagnostic signal. A new design of the filter stack recipe implemented in this work, prioritizes the Compton electrons produced in the high-Z materials to produce more discerning signals that may be unfolded with greater accuracy (see Fig. 1(d))²⁸.

A MACOR (glass-ceramic) screen, which functioned as a diffuse reflector, was used to capture the reflected light off of the target. The screen is 28 \times 28 cm, and turned to 50 $^\circ$, 36.5 cm away from the target. The MACOR screen captures the majority of the back-reflected light, and thus can be used to make qualitative observations about laser-target coupling between various targets. A camera outside of the chamber triggered at laser time, with a 10 ms exposure images this screen with a zoom lens.

III. EXPERIMENTAL RESULTS

A. Laser-target coupling

Energy and peak intensity incident on each target wheel is detailed in Table I. Each type of target was shot six times in a single vacuum pump cycle. An example crater from a shot on bare Ta is featured in Fig. 3.

TABLE I. Average Laser Parameters

Target	Energy (J)	Pulse duration (fs)	I_p ($\times 10^{21}$ W/cm 2)
Bare	5.43 ± 0.36	50	3.45 ± 0.23
Plastic	5.97 ± 0.45	60	3.16 ± 0.24
Foam	6.70 ± 0.34	45	0.51 ± 0.03^a
NWs	6.29 ± 0.37	47	3.85 ± 0.23^b

^a Lower intensity at surface of foam due to focusing on substrate.

^b Intensity on surface of NWs is lower but cannot be calculated due to NW geometry.

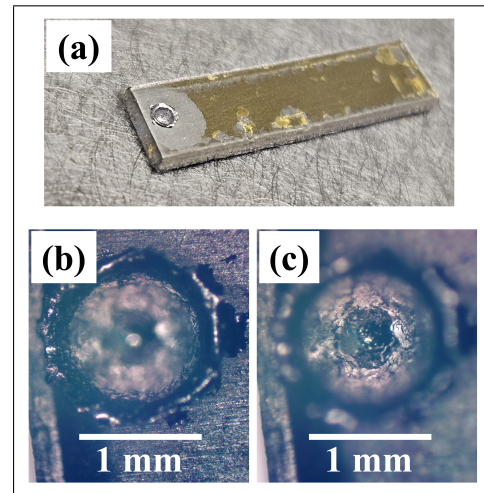


FIG. 3. (a) Example crater on plastic-coated Ta. Ta strip is 5 \times 20 \times 1 mm. Crater on bare Ta target with the (b) surface in focus, (c) bottom of crater in focus. Both crater depth and diameter varied with the target tested. Note that the focal spot had a $1/e^2$ diameter of 4.2 μm

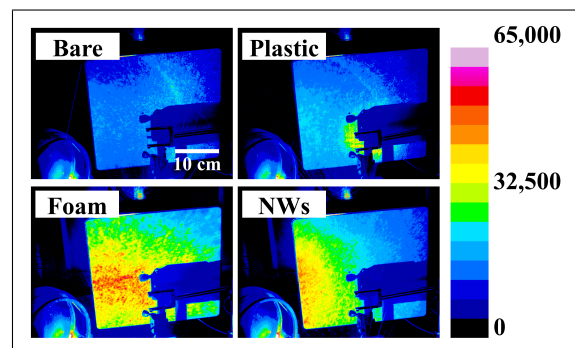


FIG. 4. Representative MACOR images for all samples tested. The $f/2$ focusing optic is in the bottom left of each image. The microscope objective used for front-side imaging is casting a shadow on the MACOR screen, and partially obscuring the front CR-39. MACOR images of NWs were the most variable in intensity.

Images obtained from the MACOR screen are featured in Fig. 4. Only the NW targets generated variable MACOR images, with half of the shots saturating the screen (camera had ND=1.9). Other target types tested produced similar back-reflected scatter on each shot. A blackfly camera (BFS-U3-120S4M-CS) with a zoom lens imaged the MACOR screen,

and was located outside of the chamber, 154 cm from the screen. The camera was angled at 45° downwards. Due to saturation of the screen, and its location in the chamber, quantitative measurements of absorbed energy in the target cannot be calculated; however, qualitatively, bare and plastic-coated targets appeared to have absorbed more laser energy than the nanostructured targets.

Post-damage crater morphology reveals that crater size varies with target type, and crucially agrees with images of the MACOR screen. Average crater diameter, depth, and estimated volume are detailed in Table II. The volume is obtained with the ellipsoid volume equation: $V = (4/3)\pi abc$, where a, b, c are the three radii of the crater. This estimated crater volume is half of the calculated ellipsoid value, since the crater is a hemisphere. Crater depth is measured with a Mitutoyo 543-793-10 digimatic indicator. The MACOR images with the lowest signal features the greatest absorption by the target, also had the largest crater diameters. Additionally, the two brightest MACOR images from the NW-coated targets had the lowest crater diameters measured at 0.56 ± 0.03 mm. This relationship between MACOR signal and crater size is further detailed in the supplementary materials, Fig. s2.

At high intensities, a phase explosion may occur in which an overheated surface region of the melt layer decomposes into vapor and liquid droplets²⁹. In this regime the surface layer in the highest-fluence region becomes thermodynamically unstable and releases a mixture of vapor and droplets, while material removal outside the central, highest-fluence region is often governed by photomechanical processes (spallation) driven by relaxation of laser-induced stresses^{29,30}. Because ultrashort pulses deposit energy into a very shallow absorption region set by the optical absorption depth and the ballistic transport of excited electrons, the initial vapor/plasma formation of phase explosion is confined to a thin surface layer (nm–100s nm, depending on material and fluence), whereas deeper material is typically melted and then ejected as droplets or spalled chunks rather than being converted to vapor^{29,31}. Material removal deeper into the crater can also involve laser-driven hole boring. Hole boring arises when the radiation pressure (ponderomotive force) of the laser pushes the critical-density surface inward, driving a collisionless shock into the plasma and accelerating ions³². In this process, the laser-driven plasma layer acts like a piston pushing into the material. At sufficiently high intensities, relativistic transparency can modify the hole-boring dynamics by allowing the laser to propagate deeper into the overdense plasma. High-intensity hole boring in the incomplete hole-boring regime (where the piston velocity is insufficient to expel the entire target thickness before the laser pulse ends) is associated with increased fast-ion cutoff energies³².

TABLE II. Average Crater Dimensions versus Target Type

Target	Diameter (mm)	Depth (mm)	Volume (mm ³)	Energy Abs. (J)
Bare	1.46 ± 0.08	0.48 ± 0.05	0.51 ± 0.04	5.03 ± 0.38
Plastic	1.52 ± 0.09	0.56 ± 0.09	0.64 ± 0.18	6.36 ± 1.80
Foam	1.24 ± 0.07	0.42 ± 0.02	0.32 ± 0.04	3.22 ± 0.37
NWs	0.95 ± 0.34	0.34 ± 0.13	0.23 ± 0.20	2.30 ± 1.95

Energy absorbed in Table II can be obtained by using the specific heat of tantalum, 25.36 J/mol K at 298 K, and the heat of fusion, 31.4 kJ/mol³³, to approximately estimate the minimum required energy required to melt this volume of material. These estimates neglect 1) the vaporized surface layer of the material (10s to 100s of nm²⁹) in a phase explosion, 2) mechanically ejected fragments produced by subsurface void nucleation and growth during the relaxation of high thermoelastic stresses under stress-confinement conditions³¹, and 3) Coulomb explosion, where a positively charged surface left by the laser ionization and the neutralization by free electrons from the bulk³⁰. If we had assumed thermal equilibrium, with the material boiling off into vapor, the energy required to vaporize this amount of material would require 35.25 ± 2.68 J for the bare targets. This is evidence that the material ejected or removed from the crater is not due to a thermal process.

B. Electrons

Featured is the electron spectra obtained from the eWASP (Fig. 5) as well as the average electron temperature obtained from fitting to an exponential distribution: $f \approx \exp(-E/T)$ (Table III) where E is the electron energy and T is the derived temperature. The average electron temperatures were obtained using the bottom and back IPs of the eWASP, which captured electrons up to ~ 50 MeV. Due to the distance from the target to the detector of 33.8 cm, only $\pm 1.5^\circ$ could be observed. The eWASP could not be closer to the target due to routine focal spot imaging.

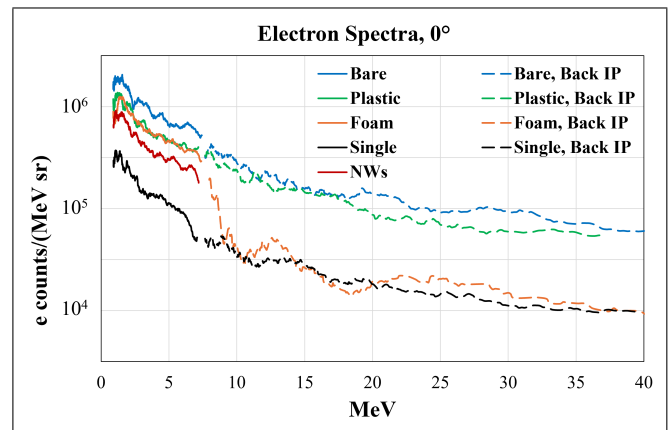


FIG. 5. Electron spectra taken at 0° , directly along the laser axis. The dashed line is the same target wheel, but the back IP instead of the bottom. A single pump shot on bare Ta is featured. The back IP for the foam target may have been loaded incorrectly into the detector. The back IP for the NW target was not loaded correctly and is not shown.

Total number of electrons incident on the eWASP was highest for the bare targets, as the IP had to be scanned 14 times to remove saturation. The plastic-coated targets had the next highest electron count, and the IP had to be scanned 9 times. Finally the foam and NW targets both needed to be scanned 6 times, and produced the fewest electrons on the eWASP. The

spectra in Fig. 5 are scaled according to the number of times the particular IP scanned as the IP lost $\sim 10\%$ signal each time it was scanned.

C. MeV X-rays

While the electrons measured by the eWASP reveals information regarding the laser-plasma acceleration processes, the electrons accelerated near the front surface of the target are depleted as they traverse the 1 mm Ta target. Additional information can be recovered by assessing the secondary X-rays produced via bremsstrahlung processes. The challenge occurs with the recovery of the spectrum. Conventional techniques for keV X-rays such as crystal-based spectrometers and X-ray streak cameras, become ineffective at MeV levels. Diagnostics that have effectiveness in this MeV range, such as Compton-based spectrometers and single-photon counting cameras, require fluxes that are either too high or too low, respectively, for the flux space occupied by laser-driven sources. To address these issues, a diagnostic routine has been developed utilizing the FSS and a perturbative minimization unfolding algorithm to recover the spectrum²⁸.

Typical attenuation-based X-ray diagnostics rely on a series of filters and image plates to attenuate photons of different energies in different amounts from which a response matrix can be built using particle transport codes, such as Monte Carlo N-Particle Transport (MCNP) code³⁴. The raw photostimulated luminescence (PSL) signal in conjunction with the characteristic response matrix may then be used to unfold the spectrum by solving the inverse of the following $\sum S_i RM_{ij} = PSL_j$, where S is the vector containing counts in the X-ray spectrum, and RM is the response matrix for the FSS²⁸. Although this is effective in the keV range, in the MeV range the mass-attenuation coefficients flatten out, making it difficult to discriminate between photons of different energies, resulting in an ill-conditioned matrix. A more extensive discussion is detailed by Wong et al.²⁸.

The work presented here builds on previous studies involving the Filter Stack Spectrometer (FSS). Typically, to differentially filter the X-ray signal, low-Z and high-Z materials are placed towards the front and back of the stack, respectively. A byproduct of MeV photon interactions with these high-Z filters is the generation of Compton electrons. While these electrons are typically accounted for in MCNP calculations, their potential has not been fully utilized. Recent work has shown that a filter stack specifically designed to generate electrons consistently throughout the stack can result in a response matrix that is better conditioned and subsequent unfolding of a higher-fidelity X-ray spectrum⁹. The response matrix from this Compton-based X-ray spectrometer is shown in the supplementary materials (Fig. s3).

The raw PSL signal and MeV X-ray spectra from the different target types via our unfolding routine can be found in Fig. 6(a) and Fig. 6(b), respectively. Dose per total shot energy for bare, plastic-coated, foam-coated, and NW-coated are 4.2×10^{-6} rad @1m/J sr, 3.3×10^{-6} rad @1m/J sr, 3.0×10^{-6} rad @1m/J sr, and 3.0×10^{-6} rad @1m/J sr respec-

tively.

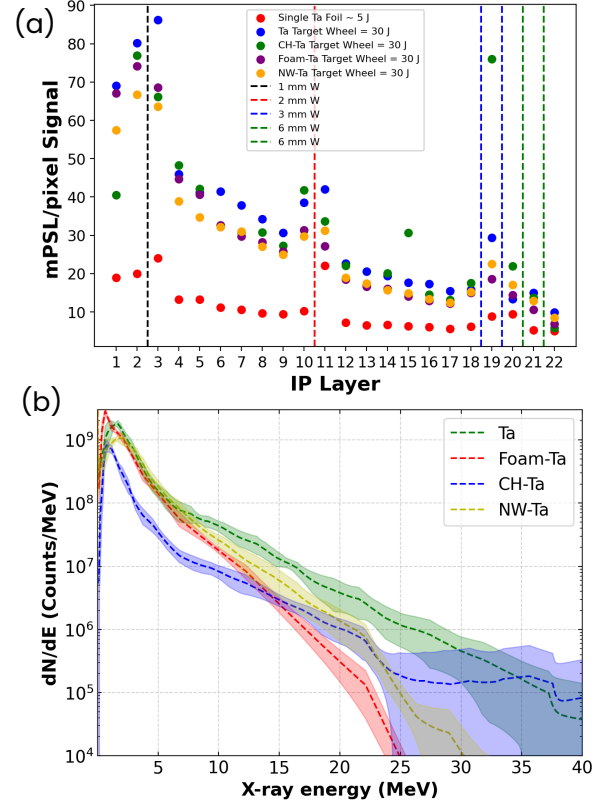


FIG. 6. (a) The raw PSL per pixel signal is shown for the different target types. The vertical dashed lines represent the W filters, which act as intensifiers via the production of Compton electrons. The enhanced signal from the back and forward scatter electrons is apparent. (b) Final X-ray spectrum. The unfolding routine uses the PSL data to recover the X-ray spectrum.

D. Ta ions

The main results from the attenuated CR-39 is featured in Fig. 7 and Table V. CR-39 was positioned in front of the MACOR screen in the reflected direction off the target, and behind the targets; however, most of the front CR-39 was obstructed by a microscope objective used for sample alignment and the only exposed part did not have any mylar shielding. These CR-39 were saturated, but sections were counted by hand to provide a low-end estimate for total ion counts. The front CR-39 for the single shot on bare Ta was also saturated. Front CR-39 was located 33 cm from the target, at an angle of $\sim 48^\circ$, while the back CR-39 was 31 cm from the target.

The mylar thicknesses were chosen to be able to discern Ta ion energies via SRIM (Stopping and Range of Ions in Matter), with 12 μm mylar allowing ions > 45 MeV through. The energy cutoff for each thickness of mylar is featured in Table IV. Proton energies could not be differentiated because of this inadequate shielding, but could theoretically be counted under optical microscope. Counting of protons would require

TABLE III. Fitted Electron Temperatures

Angle (°)	Bare, T(MeV)	Plastic, T(MeV)	Foam, T(MeV)	NWs, T(MeV)	Single Bare ^a , T(MeV)
-1.50	5.30 ± 0.21	5.12 ± 0.20	5.19 ± 0.17	4.37 ± 0.17	4.80 ± 0.19
-0.75	5.07 ± 0.21	4.24 ± 0.15	4.74 ± 0.15	4.06 ± 0.16	3.62 ± 0.12
0	4.81 ± 0.22	3.93 ± 0.14	4.72 ± 0.17	3.48 ± 0.14	3.62 ± 0.12
0.75	4.87 ± 0.20	4.41 ± 0.15	4.75 ± 0.16	3.68 ± 0.13	3.55 ± 0.11
1.50	5.00 ± 0.20	4.78 ± 0.21	5.89 ± 0.23	4.59 ± 0.21	4.85 ± 0.21
Average	5.01 ± 0.21	4.50 ± 0.17	5.06 ± 0.18	4.03 ± 0.16	4.09 ± 0.15
Average, Back IP (T _{hot})	17.77 ± 0.94	15.22 ± 0.77	10.63 ^b ± 0.99	-	17.63 ± 1.30

^a This is from a single bare target, instead of six.

^b The specific IP may have been loaded incorrectly into the eWASP

50x magnification instead of the 10x used for the ions. Unfortunately, this range of mylar thickness also allows C ions to be differentiated between 0.35-12 MeV. As the front of the target was coated, the front CR-39 likely detected more C ions, these could have been differentiated by multi-step etching.

TABLE IV. Mylar attenuation of Ta ions from CR-39 positioned behind the target

Mylar thickness (μm)	Allowed energies (MeV)
0	> 0 MeV
1	> 2.5 MeV
3	> 7.0 MeV
6	> 16.0 MeV
9	> 27.5 MeV
12	> 45.0 MeV

Foam and NW-coated targets exhibited an even spread of ions across the 5.1×5.1 cm CR-39, while bare and plastic-coated targets had clear regions of heightened ion density. The reported ion counts in Table V are all the pits for the entire back CR-39, while three representative microscopy images at 50x were used to estimate total counts for the front CR-39 of each target tested.

IV. PARTICLE-IN-CELL SIMULATION

We performed two-dimensional (2D) particle-in-cell (PIC) simulations using version 4.17.10 of the EPOCH code³⁵, modeling both bare Ta target and Ta coated with a plastic layer. The schematic setup for both simulations is shown in the supplementary materials, where the pulse is injected at 28° with a central wavelength of $\lambda = 0.8 \mu\text{m}$, temporal sin^2 FWHM $\tau = 50$ fs, $1/e^2$ radius of $\Omega_0 = 3 \mu\text{m}$, and a peak intensity of $3 \times 10^{21} \text{ W/cm}^2$. A $10 \mu\text{m}$ thick bulk Ta is used to represent the bare Ta case, while a $1 \mu\text{m}$ thick plastic coating consisting of carbon (C) and hydrogen (H) is added before Ta to represent the plastic-coated Ta. The pulse is on for a 2τ window from $t = 0$ fs. Due to computational constraints, we are unable to model the full 1 mm thick tantalum (Ta) target used in the experiment. Additionally, the thickness of the plastic layer is set to $1 \mu\text{m}$ to ensure that it exceeds the laser

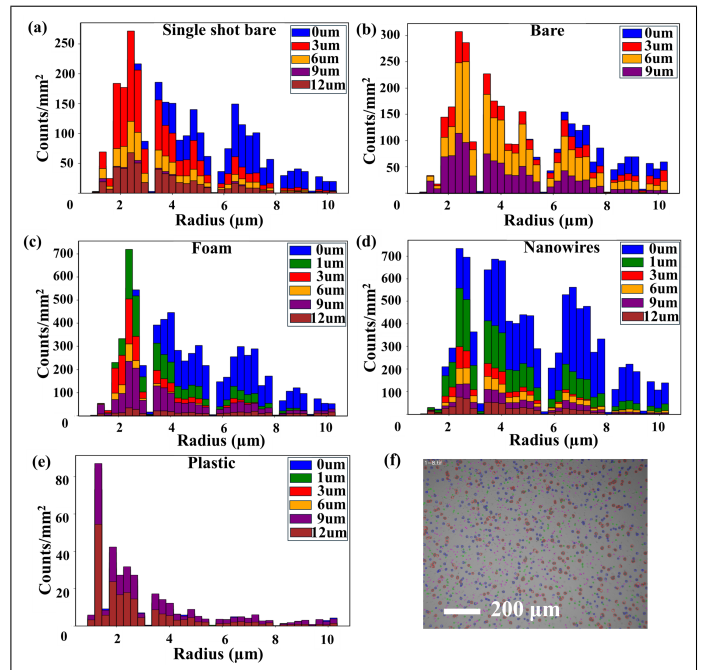


FIG. 7. (a)-(e) Experimental counts of Ta ions, with each pit radius measured by a machine-learning technique. Each CR-39 was exposed for six shots on each target type (except the single shot bare), with different thicknesses of mylar to differentiate Ta ions based on energy. (f) Example microscope image of rear CR-39 with the pits counted.

wavelength λ , and therefore properly represents the interaction with the laser field.

The material number densities and band gaps used in the simulations are summarized in Table VI. For simplicity, each plastic molecule is assumed to consist of two carbon atoms and four hydrogen atoms, although the actual composition of AZ nLOF 2070 may also include nitrogen (N) and oxygen (O). Tantalum (Ta), which has 73 electrons, cannot be fully ionized within the computational constraints of the simulation. Instead, only the first four ionization states (i.e. $Z=4$) are included to capture the representative physics and key phenomena. Similarly, for the plastic material, each constituent atom is assumed to ionize up to one electron to simplify the modeling of plasma formation.

TABLE V. Ion counts/sr J [$\times 10^7$]

Target	Front 0 μm	Back 0 μm	1 μm	3 μm	6 μm	9 μm	12 μm
Single Shot Bare	-	4.3	-	3.0	1.6	0.80	0.80
Bare	$> 10.3 \times 10^3$	4.6	-	5.2	4.2	1.8	-
Plastic	$> 4.2 \times 10^3$	0.56	0.47	0.42	0.44	0.59	0.32
Foam	$> 2.3 \times 10^3$	9.5	6.3	4.1	2.7	2.6	0.58
NWs	$> 4.7 \times 10^3$	17	8.4	4.2	3.3	2.1	1.1

These simplifications may underestimate the total electron density and overestimate the average electron energy. However, they preserve the essential plasma dynamics while ensuring computational feasibility. To complement this approach, an additional simulation is performed for bare Ta with the maximum charge state extended to Ta^{21+} , corresponding to ionization energies up to about 600 eV, to assess the effects of higher ionization on plasma behavior.

TABLE VI. Material Properties.^{36–38}

Material	Ionization Energy (eV)	Number Density (cm^{-3})
Ta	7.55, 16.17, 23.11, 35.03	$5.55\text{e}+22$
H	13.6	$8.24\text{e}+22$
C	13.6	$4.12\text{e}+22$

The simulations for Ta with four ionization states use a spatial resolution of 12 nm in both directions, while the simulation for Ta with 21 ionization states uses resolutions of 7 nm in the x direction and 10 nm in the y direction. All simulations are initialized with 100 neutral macroparticles per cell for each species at a temperature of 298 K. For each simulation, we use the default time step in 2D EPOCH of 0.95 times the Courant–Friedrichs–Lewy (CFL) limit^{35,39,40}.

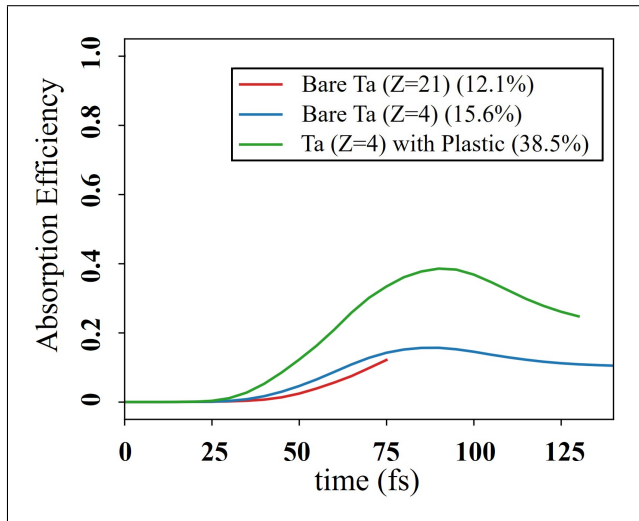


FIG. 8. Absorption efficiency for bare Ta($Z=21$), bare Ta($Z=4$), and Ta($Z=4$) with plastic coating, with the maximum efficiency 12.1%, 15.6%, 38.5%, respectively. The bare Ta has an absorption peak slightly earlier than plastic-coated.

The absorption efficiency for all particle species in the three cases is shown in Fig. 8. For bare Ta with 21 ionization states, the extremely large number of electron species significantly increases the computational cost, requiring nearly 35 hours of computation for every 5 fs simulated. This makes it impractical to complete the entire simulation within reasonable time and resource constraints. Therefore, we paused the simulation for Ta ($Z=21$) at 75 fs, as the most energetic electrons in the simulations of both bare Ta ($Z=4$) and Ta with plastic coating appear by 70 fs.

In addition, the absorption differs by only about 2–3% between $Z=4$ and $Z=21$ for bare Ta, which aligns with our expectation since a larger number of electrons leads to more energy being consumed in ionization processes rather than being absorbed. The relatively small difference also suggests that limiting the simulation to the first four ionization states of Ta may still provide an acceptable quantitative approximation of the overall absorption behavior, despite Ta having up to 73 possible ionization states.

For Ta ($Z=4$) with plastic coating, the total energy absorbed by all particle species is about 38.5% of the pulse energy. Beyond the energy absorbed by C and H atoms and their electrons, the absorption only by Ta ions and electrons reaches approximately 28.8%, still nearly double that of bare Ta. The ion absorption is about 0.6%, 0.9%, and 1.0% for bare Ta ($Z=21$), bare Ta ($Z=4$), and Ta with plastic, indicating that most of the laser energy is absorbed by electrons in these simulations. The absorption efficiency starts to decrease after about 80 fs, as those most energetic electrons leave the simulation box.

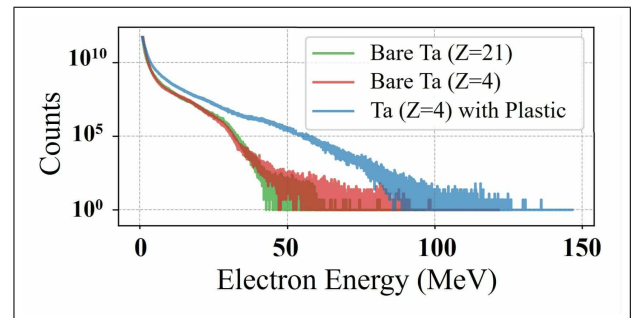


FIG. 9. Ta electron spectrum for bare Ta($Z=21$), bare Ta($Z=4$), and Ta($Z=4$) with Plastic coating at 70 fs (when most energetic electrons are observed). In the experimental electron spectra, the bare and plastic-coated Ta produce similar spectra past 30 MeV, with bare Ta generating more electron acceleration.

In Fig. 9, the Ta electron energy spectra at 70 fs for the three

cases are presented. Below approximately 60 MeV, the spectra of bare Ta ($Z=21$) and bare Ta ($Z=4$) overlap closely. However, for energies above 60 MeV, more electrons gain higher energies in the $Z=4$ Ta case, with the maximum energy reaching about 98 MeV, compared to approximately 82 MeV for the $Z=21$ case. A turning point is observed around 30 MeV for both cases. For Ta with plastic coating, a generally higher number of electrons gain energy across the entire range, with maximum energy reaching about 136 MeV, indicating an enhancement in energy absorption due to the presence of the plastic layer.

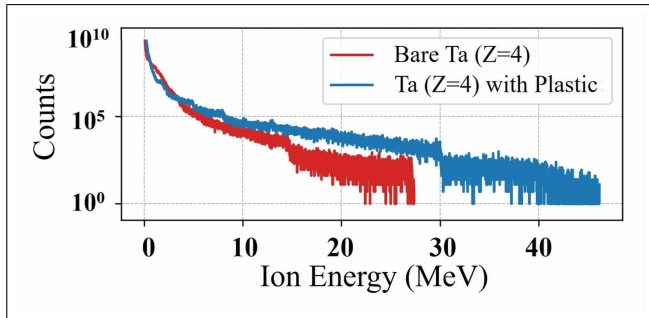


FIG. 10. Ta ion spectrum for bare Ta($Z=4$), and Ta($Z=4$) with Plastic coating at 125 fs (when most energetic ions are observed).

In Fig. 10, the energy spectra of Ta ions with a 4+ charge state at 125 fs are presented, corresponding to the time when the most energetic ions are observed. It can be seen that, with the plastic coating, there are more ions across the entire energy range above approximately 3 MeV, with the maximum ion energy reaching about 46 MeV. In contrast, for bare Ta, the ion energy extends only up to around 27 MeV. After approximately 150 fs, the maximum ion energies stabilize at around 15 MeV for bare Ta and 30 MeV for Ta with plastic. The energetic electrons transfer energy to the ions as they are pushed into the target, so that a small quantity of ions gain a great amount of energy in a short time. This causes a sharp rise of the spectrum. This trend is also evident in Fig. 10 at 125 fs, where distinct steps appear at 15 MeV and 30 MeV for each case, respectively. These sharp features at these energies smooth out at later times.

V. DISCUSSION

The hot electrons generated by the laser-target interaction lose energy to bremsstrahlung radiation, ionization, and electron refluxing, while the highest energy electrons will escape the target⁴¹. In this experiment, laser-target coupling efficiency can be correlated between the reflected light on the MACOR screen and the post-damage craters. A greater signal on the MACOR screen signifies lower laser-target coupling. At the same time, craters measured after the experiment increase in diameter as the laser coupling increases. Measurements from PIC simulations suggest that bare Ta targets exhibited 15 % energy absorption. Greater laser-target coupling also leads to greater MeV electron and X-ray generation (Fig.

5). Absorption measurements are difficult to make and may require large diagnostics²³. Crater analysis offers a facile option in determining laser-target energy coupling.

The dominant mechanism for electron acceleration in \sim mm thick targets at relativistic intensities is $j \times B^{42}$. The hot electron temperature which is responsible for accelerating ions, can be approximated by using the ponderomotive energy scaling as⁴³:

$$T_{hot} \approx mc^2 \left(1 + \frac{2U_p}{mc^2} \right)^{1/2}, \quad (1)$$

$$U_p = 9.33 \times 10^{-14} I \lambda^2. \quad (2)$$

Where T_{hot} is the hot electron temperature, U_p is the ponderomotive potential [eV], and I is the peak intensity [W/cm^2], and λ is the laser wavelength [μm]. Using this equation for our intensities from $0.5-4 \times 10^{21} W/cm^2$, we are able to estimate the electron temperatures from 5.62-15.83 MeV. Derived T_{hot} from Table III show that the ponderomotive scaling agrees well with the experimentally derived temperature for plastic targets, but underestimates electron temperatures for bare and foam-coated targets.

Coated (high- Z) targets can offer higher laser-target energy coupling than bare targets; however, the coating should not be prematurely destroyed by near-relativistic intensities²¹. It is likely that the tested foam (or NW) thickness and density are not well suited for these intensities and pulse durations. Yin et al.⁴⁴ ran multiple simulations regarding foam thickness and density at relativistic intensities, and determined the coating should be chosen such that relativistic induced transparency in the dense plasma coincides with the peak of the pulse, in order to generate the most high energy electrons. It is also observed that too much preplasma can prevent most of the laser energy from interacting with the target⁴⁴. Yin. et al.⁴⁴ tested foam-coated tungsten targets with a BELLA-class laser⁴⁵, with similar intensity, 815 nm central wavelength and 300 fs pulse duration, and obtained the greatest electron production with 13 μm foam thickness, at 27 mg/cc. In our case, we used 50 μm thick foam with 15 mg/cc. Poor optimization of the NW-coating may also have negatively affected the resultant electron spectra. Parameters such as NW diameter, length, and spacing have an important effect on resultant electron number and temperature⁶; however, in Vallieres et al.⁶ all of their tested NW-coated targets performed better than bare foils.

Electron temperature from plastic-coated targets is slightly lowered compared to bare targets. In theory, plastic-coated targets can more effectively couple the laser energy to the target and can more readily undergo relativistic transparency¹⁷. Alternatively, an earlier heater beam can pre-ionize the plastic layer, offering a homogeneous plasma to the main pulse¹⁶. In these previous studies, a plastic layer of 2 or 10 μm was used over the high- Z Ta target^{16,17}. In our case, while the electron temperature and counts are slightly lowered, the energy absorption and X-ray emission are comparable to those of bare targets. PIC simulations suggest that a 1 μm thick plastic coating on Ta could increase coupling up to 28.8% on the Ta substrate.

Simulations from Miller et al.⁴⁶ show a strong correlation between both laser intensity and plasma scale length in producing the greatest 1-5 MeV X-ray emission. The highest intensity tested of 5×10^{20} W/cm², at 25 fs pulse duration, exhibited the greatest electron acceleration >5 MeV, while subsequently emitting the highest X-ray dose⁴⁶. While coated targets in this experiment have a larger plasma scale length, due to the focusing on the substrate, the maximum intensity at the coating surface is lower for the coated targets (by an order of magnitude for foam targets). Therefore, while bare Ta had the shortest plasma scale length, it also maintained the greatest intensity before the plasma was overcritical. Thinner or lower density coatings, as well as focusing on the surface of the coating, would likely cause all coated targets to outperform bare Ta.

For MeV X-rays, the difference in performance between the different front-surface targets is apparent. Although the X-ray yield is comparable at lower energies, a difference emerges at $E_{photons} > 5$ MeV. Similar to the eWASP measurements, the foam and nanowires suffer at higher energies, speaking to the precise laser-plasma conditions necessary to make these target types advantageous. The foam does outperform other targets from 4-8 MeV, a range that is useful for radiographic purposes, and similarly has a different spectral shape. However, the dominance of bare Ta and plastic-coated Ta at the highest energies is likely due to the enhanced laser-plasma coupling that occurs in the performed plasma. The X-rays benefit from self-focusing of the beam and relativistic induced transparency that allows the beam to penetrate into the overdense plasma, similar to past work¹⁷. Previous work by Strehlow et al.¹⁷ with a 1 μ m, 120 J, 140 fs pulse duration laser obtains 3×10^{-4} rad @ 1m/J sr on bare 1 mm Ta compared to our 4.2×10^{-6} rad @ 1m/J sr.

Target normal sheath acceleration (TNSA) is the dominant ion acceleration mechanism for $\sim \mu$ m thick solid targets⁴³, as thicker targets reduce the generated field. In this process, a cloud of electrons in the front and rear of the target accelerate ions on the front and rear side. These ions are accelerated in the normal direction from the target. Ions accelerated from the back of the target generally have higher energies, due to a sharper density gradient than the front^{43,47}. The angular divergence of the ions from the front surface should greatly exceed that of the rear surface due to a longer pre-plasma length⁴³.

The rear CR-39 was in the laser axis direction, and both front and rear CR-39 were a similar distance away from the target (33 versus 31 cm). While TNSA is most effective in accelerating protons and low-Z ions, it is still possible to accelerate mid and high-Z ions⁴², with laser to ion energy conversion efficiency of 4% reported for heavier ions⁴⁸. As the accelerated ions in the back come from the back surface, they are assumed to be Ta ions⁴³. Front CR-39 likely detected C and Au ions from the coated targets, but cannot be observed due to saturation. Front ion counts is ~ 3 orders of magnitude greater than back on the CR-39 (Table V) but likely contains lower energy particles⁴³. PIC simulations observe accelerated ions of 46 MeV from the plastic-coated Ta, which agrees with experimental results.

Coating a target with nanostructures has lead to greater ion

yields⁴⁹, but is dependent on laser energy, pulse duration, and target thickness due to risk of generation of an overcritical pre-plasma at the incorrect time. This overcritical preplasma may then shutter the main pulse interaction⁴⁹. More efficient generation of electrons to drive TNSA has been exhibited by a low density coating, like foam⁵⁰. Foam and NW-coated targets exhibit the greatest stability and quantity of accelerated ions for our laser parameters. Lower total hot electron generation but heightened ion acceleration could mean that the foam and NW targets experienced a volumetric effect⁵¹. With the laser focusing on the Ta substrate, it is possible the pulse was prematurely shuttered by these thicker coatings. Almasarani et al. observed a larger spot size can generate more ion acceleration, but lower overall max ion energies⁵¹, albeit in $\sim \mu$ m thick targets.

VI. CONCLUSION

Four different target-coating geometries were tested on Scarlet, a high contrast, ultrafast laser. Of the tested coatings, bare targets generated the greatest quantity of electron acceleration, the hottest electrons, as well as the greatest MeV X-ray production. Foam and NW-coated targets, however, did produce the greatest heavy ion acceleration. This improved ion acceleration for structured targets compared to bare Ta, is potentially due to the volumetric effect⁵¹. In previous studies, laser intensity and plasma scale length have been strongly correlated with an increase in MeV electrons and X-rays^{46,52}. While the plasma scale length for coated targets was increased, this premature shuttering of the rest of the pulse led to a decrease in intensity on the target.

The greatest MeV electron and X-ray yield has been associated with greater laser-target energy coupling. Images of the MACOR screen reveal that bare Ta and plastic-coated Ta had the greatest laser-target energy absorption. Qualitative measurements about laser absorption from the MACOR agree with post-damage crater diameter. The crater diameter decreased from 1.46 ± 0.08 mm, to 0.95 ± 0.33 mm from the bare Ta to the NW-coated Ta. Particle-in-cell simulations suggest that bare Ta absorbs 15% of the laser energy. The shots on NW-coated Ta with the greatest MACOR signal correspond to the smallest diameter craters. Absorption measurements are difficult to carry out and may require a large diffuse reflector or an Ulbricht sphere²³. Post-damage crater analysis is an easy way to compare absorption between target types. Future studies may be able to further study the diameter of craters alongside a diffuse reflector, and compare the absorption measurements to particle-in-cell simulations.

While bare targets perform the best, particle-in-cell simulations suggest that 1 μ m plastic-coating would perform better than bare Ta substrate. Due to the Rayleigh length of the focus, a coating $< 8 \mu$ m would likely perform better than bare Ta, when focusing the laser on the substrate. The 50 μ m thick foam coating with 15 mg/cc was either too thick or too dense for the focusing geometry. The foam or NW target may have also coupled more laser energy if the laser was focused on the coating. Focusing geometry, laser wavelength,

pulse duration, and laser contrast should be carefully considered before selecting a target coating, in order to produce the greatest heavy ion and MeV X-ray emission from specific laser sources. These results showcase particle emission from a high-contrast, short pulse, high-power system, and offer a facile way to benchmark absorption for different targets.

SUPPLEMENTARY MATERIALS

See the supplementary materials for the following: Figure s1, Scanning Electron Microscope (SEM) images of the foam and NW-coated targets. Figure s2, MACOR signal variation and subsequent changes to crater morphology. Figure s3, response matrix used for the FSS unfolding. Figure s4, particle-in-cell simulation setup diagram. Figure s5, electron density and temperature 70 fs after irradiation modeled in particle-in-cell.

ACKNOWLEDGMENTS

Partial funding for shared facilities used in this research was provided by the Center for Emergent Materials: an NSF MR-SEC under award number DMR-2011876.

DATA AVAILABILITY STATEMENT

Data taken and used for this paper is available upon request from the primary author.

REFERENCES

- ¹C. Courtois, R. Edwards, A. Compant La Fontaine, C. Aedy, M. Barbotin, S. Bazzoli, L. Biddle, D. Brebion, J. Bourgade, D. Drew, *et al.*, “High-resolution multi-mev x-ray radiography using relativistic laser-solid interaction,” *Physics of Plasmas* **18** (2011).
- ²S. Singh, C. D. Armstrong, N. Kang, L. Ren, H. Liu, N. Hua, D. R. Rusby, O. Klimo, R. Versaci, Y. Zhang, *et al.*, “Bremsstrahlung emission and plasma characterization driven by moderately relativistic laser-plasma interactions,” *Plasma Physics and Controlled Fusion* **63**, 035004 (2021).
- ³S. Wilks, W. Kruer, M. Tabak, and A. Langdon, “Absorption of ultra-intense laser pulses,” *Physical review letters* **69**, 1383 (1992).
- ⁴G. Malka and J. Miquel, “Experimental confirmation of ponderomotive-force electrons produced by an ultrarelativistic laser pulse on a solid target,” *Physical review letters* **77**, 75 (1996).
- ⁵D. Jung, R. Hörlein, D. Gautier, S. Letzring, D. Kiefer, K. Allinger, B. Albright, R. Shah, S. Palaniyappan, L. Yin, *et al.*, “A novel high resolution ion wide angle spectrometer,” *Review of Scientific Instruments* **82** (2011).
- ⁶S. Vallières, M. Salvadori, A. Permogorov, G. Cantono, K. Svendsen, Z. Chen, S. Sun, F. Consoli, E. d’Humières, C.-G. Wahlström, *et al.*, “Enhanced laser-driven proton acceleration using nanowire targets,” *Scientific Reports* **11**, 2226 (2021).
- ⁷H. Chen, S. C. Wilks, J. D. Bonlie, S. Chen, K. Cone, L. Elberson, G. Gregori, D. D. Meyerhofer, J. Myatt, D. Price, *et al.*, “Making relativistic positrons using ultraintense short pulse lasers,” *Physics of Plasmas* **16** (2009).
- ⁸J. Strehlow, C.-S. Wong, S. V. Luedtke, A. Bogale, A. F. Bengoa, R. Fitzgarrald, L. T. Mix, R. Nedbailo, D. R. Rusby, J. L. Schmidt, *et al.*, “Filter stack spectrometer measurements of high energy x-ray sources for radiography,” *Nuclear Instruments and Methods in Physics Research Section A: Accelerators, Spectrometers, Detectors and Associated Equipment* **1076**, 170465 (2025).
- ⁹A. S. Bogale, L. Yin, S. Palaniyappan, J. Strehlow, S. V. Luedtke, C.-S. Wong, D. Stark, D. C. Gautier, J. C. Fernandez, A. V. Pelt, L. T. Mix, J. Twardowski, R. Fitzgarrald, F. N. Beg, and B. J. Albright, “Optimizing mev photon dose generation in laser–solid interactions via stable beam propagation,” *Physical Review Research* **7**, 023169 (2025).
- ¹⁰J. C. Fernández, D. Cort Gautier, C. Huang, S. Palaniyappan, B. J. Albright, W. Bang, G. Dyer, A. Favalli, J. F. Hunter, J. Mendez, *et al.*, “Laser-plasmas in the relativistic-transparency regime: Science and applications,” *Physics of plasmas* **24** (2017).
- ¹¹S. Bulanov, T. Z. Esirkepov, V. Khoroshkov, A. Kuznetsov, and F. Pegoraro, “Oncological hadrontherapy with laser ion accelerators,” *Physics Letters A* **299**, 240–247 (2002).
- ¹²F. Fiúza, A. Stockem, E. Boella, R. Fonseca, L. Silva, D. Haberberger, S. Tochitsky, C. Gong, W. B. Mori, and C. Joshi, “Laser-driven shock acceleration of monoenergetic ion beams,” *Physical Review Letters* **109**, 215001 (2012).
- ¹³M. Borghesi, D. Campbell, A. Schiavi, M. Haines, O. Willi, A. MacKinnon, P. Patel, L. Gizzi, M. Galimberti, R. Clarke, *et al.*, “Electric field detection in laser-plasma interaction experiments via the proton imaging technique,” *Physics of Plasmas* **9**, 2214–2220 (2002).
- ¹⁴M. Roth, D. Jung, K. Falk, N. Guler, O. Deppert, M. Devlin, A. Favalli, J. Fernandez, D. Gautier, M. Geissel, *et al.*, “Bright laser-driven neutron source based on the relativistic transparency of solids,” *Physical review letters* **110**, 044802 (2013).
- ¹⁵V. Verma, M. V. Mishra, and M. P. Mehta, “A systematic review of the cost and cost-effectiveness studies of proton radiotherapy,” *Cancer* **122**, 1483–1501 (2016).
- ¹⁶C. Courtois, A. Compant La Fontaine, O. Landoas, G. Lidove, V. Méot, P. Morel, R. Nuter, E. Lefebvre, A. Boscheron, J. Grenier, *et al.*, “Effect of plasma density scale length on the properties of bremsstrahlung x-ray sources created by picosecond laser pulses,” *Physics of Plasmas* **16** (2009).
- ¹⁷J. Strehlow, L. Yin, C.-S. Wong, S. Luedtke, S. Palaniyappan, D. Stark, C.-K. Huang, A. Bogale, B. Cage, T. Coffman, *et al.*, “Mev x-ray production from a petawatt laser in the regime of a relativistically transparent pre-plasma, with applications to radiography,” *Physics of Plasmas* **31** (2024).
- ¹⁸C. Courtois, R. Edwards, A. Compant La Fontaine, C. Aedy, S. Bazzoli, J. Bourgade, J. Gazave, J. Lagrange, O. Landoas, L. L. Dain, *et al.*, “Characterisation of a mev bremsstrahlung x-ray source produced from a high intensity laser for high areal density object radiography,” *Physics of Plasmas* **20** (2013).
- ¹⁹S. Palaniyappan, B. M. Hegelich, H.-C. Wu, D. Jung, D. C. Gautier, L. Yin, B. J. Albright, R. P. Johnson, T. Shimada, S. Letzring, *et al.*, “Dynamics of relativistic transparency and optical shuttering in expanding overdense plasmas,” *Nature Physics* **8**, 763–769 (2012).
- ²⁰M. A. Purvis, *Relativistic plasma nano-photonics for ultra-high energy density physics*, Doctoral dissertation, Colorado State University (2014).
- ²¹X. Li, X. Yang, G. Zhang, Y. Ma, J. Jiao, F. Shan, P. Han, L. Ma, M. Peng, and J. Feng, “High absorption efficiency by high intensity laser irradiating carbon aerogel targets,” *Physics of Plasmas* **29** (2022).
- ²²Y. Wu, G. Jain, T. Sizyuk, X. Wang, and A. Hassanein, “Dynamics of laser produced plasma from foam targets for future nanolithography devices and x-ray sources,” *Scientific Reports* **11**, 13677 (2021).
- ²³E. Eftekhari-Zadeh, M. Blümcke, Z. Samsonova, R. Loetzsch, I. Uschmann, M. Zapf, C. Ronning, O. Rosmej, D. Kartashov, and C. Spielmann, “Laser energy absorption and x-ray generation in nanowire arrays irradiated by relativistically intense ultra-high contrast femtosecond laser pulses,” *Physics of Plasmas* **29** (2022).
- ²⁴L. Cao, Y. Gu, Z. Zhao, L. Cao, W. Huang, W. Zhou, X. He, W. Yu, and M. Yu, “Enhanced absorption of intense short-pulse laser light by subwavelength nanolayered target,” *Physics of Plasmas* **17** (2010).
- ²⁵P. Tavana, N. Bukharskii, M. Gyrdymov, U. Spillmann, Ş. Zähler, J. Cikhart, N. Borisenko, P. Korneev, J. Jacoby, C. Spielmann, *et al.*, “Ultra-high efficiency bremsstrahlung production in the interaction of direct laser-accelerated electrons with high-z material,” *Frontiers in Physics* **11**, 1178967 (2023).

- ²⁶M. A. Purvis, V. N. Shlyaptsev, R. Hollinger, C. Bargsten, A. Pukhov, A. Prieto, Y. Wang, B. M. Luther, L. Yin, S. Wang, *et al.*, “Relativistic plasma nanophotonics for ultrahigh energy density physics,” *Nature photonics* **7**, 796–800 (2013).
- ²⁷N. Izumi, R. Snively, G. Gregori, J. Koch, H.-S. Park, and B. Remington, “Application of imaging plates to x-ray imaging and spectroscopy in laser plasma experiments,” *Review of Scientific Instruments* **77** (2006).
- ²⁸C.-S. Wong, J. Strehlow, D. P. Broughton, S. V. Luedtke, C.-K. Huang, A. Bogale, R. Fitzgarrald, R. Nedbailo, J. L. Schmidt, T. R. Schmidt, *et al.*, “Robust unfolding of mev x-ray spectra from filter stack spectrometer data,” *Review of Scientific Instruments* **95**, 023301 (2024).
- ²⁹C. Wu and L. V. Zhigilei, “Microscopic mechanisms of laser spallation and ablation of metal targets from large-scale molecular dynamics simulations,” *Applied Physics A* **114**, 11–32 (2014).
- ³⁰M. V. Shugaev, C. Wu, O. Armbruster, A. Naghilou, N. Brouwer, D. S. Ivanov, T. J.-Y. Derrien, N. M. Bulgakova, W. Kautek, B. Rethfeld, *et al.*, “Fundamentals of ultrafast laser–material interaction,” *Mrs Bulletin* **41**, 960–968 (2016).
- ³¹L. V. Zhigilei and B. J. Garrison, “Microscopic mechanisms of laser ablation of organic solids in the thermal and stress confinement irradiation regimes,” *Journal of Applied Physics* **88**, 1281–1298 (2000).
- ³²S. Weng, M. Murakami, P. Mulser, and Z. Sheng, “Ultra-intense laser pulse propagation in plasmas: from classic hole-boring to incomplete hole-boring with relativistic transparency,” *New Journal of Physics* **14**, 063026 (2012).
- ³³M. W. Chase *et al.*, “Nist-janaf thermochemical tables,” *Journal of physical and chemical reference data* **28**, 1951 (1998).
- ³⁴C. J. Werner, J. C. Armstrong, F. B. Brown, J. S. Bull, L. Casswell, L. J. Cox, D. A. Dixon, R. A. F. III, J. T. Goorley, H. G. H. III, *et al.*, “MCNP User’s Manual Code Version 6.2,” Tech. Rep. LA-UR-17-29981 (Los Alamos National Laboratory, 2017) Los Alamos National Laboratory Report.
- ³⁵T. D. Arber, K. Bennett, C. S. Brady, A. Lawrence-Douglas, M. G. Ramsay, N. J. Sircombe, P. Gillies, R. G. Evans, H. Schmitz, A. R. Bell, and C. P. Ridgers, “Contemporary particle-in-cell approach to laser-plasma modelling,” *Plasma Physics and Controlled Fusion* **57**, 113001 (2015).
- ³⁶A. Kramida, Yu. Ralchenko, J. Reader, and NIST ASD Team, NIST Atomic Spectra Database (ver. 5.12), [Online]. Available: <https://physics.nist.gov/asd> [2025, July 14]. National Institute of Standards and Technology, Gaithersburg, MD. (2024).
- ³⁷J. W. Arblaster, *Selected Values of the Crystallographic Properties of the Elements* (ASM International, Materials Park, Ohio, 2018) 1 online resource (xiii, 684 pages).
- ³⁸D. R. Lide, *CRC handbook of chemistry and physics: a ready-reference book of chemical and physical data* (CRC press, 1995).
- ³⁹R. Courant, K. Friedrichs, and H. Lewy, “Über die partiellen Differenzgleichungen der mathematischen Physik,” *Mathematische Annalen* **100**, 32–74 (1928).
- ⁴⁰R. Courant, K. Friedrichs, and H. Lewy, “On the partial difference equations of mathematical physics,” *IBM Journal of Research and Development* **11**, 215–234 (1967).
- ⁴¹S. Morris, A. Robinson, and C. Ridgers, “Highly efficient conversion of laser energy to hard x-rays in high-intensity laser–solid simulations,” *Physics of Plasmas* **28** (2021).
- ⁴²J. Strehlow, *Optimizing laser-ion acceleration with flat and structured foils*, Doctoral dissertation, University of California San Diego (2022).
- ⁴³S. Wilks, A. Langdon, T. Cowan, M. Roth, M. Singh, S. Hatchett, M. Key, D. Pennington, A. MacKinnon, and R. Snively, “Energetic proton generation in ultra-intense laser–solid interactions,” *Physics of plasmas* **8**, 542–549 (2001).
- ⁴⁴L. Yin, S. Luedtke, D. Stark, C.-K. Huang, B. Medina, A. Seaton, A. Bogale, J. Strehlow, S. Palaniyappan, L. Mix, *et al.*, “Advances in laser-based bremsstrahlung x-ray sources. i. optimizing laser-accelerated electrons,” *Physics of Plasmas* **31** (2024).
- ⁴⁵W. Leemans, R. Duarte, E. Esarey, S. Fournier, C. Geddes, D. Lockhart, C. Schroeder, C. Tóth, J.-L. Vay, and S. Zimmermann, “The berkeley lab laser accelerator (bella): A 10 gev laser plasma accelerator,” in *AIP Conference Proceedings*, Vol. 1299 (American Institute of Physics, 2010) pp. 3–11.
- ⁴⁶K. G. Miller, D. R. Rusby, A. J. Kemp, S. C. Wilks, and W. B. Mori, “Maximizing mev x-ray dose in relativistic laser–solid interactions,” *Physical Review Research* **5**, L012044 (2023).
- ⁴⁷T. Ceccotti, A. Lévy, H. Popescu, F. Réau, P. d’Oliveira, P. Monot, J. Geindre, E. Lefebvre, and P. Martin, “Proton acceleration with high-intensity ultrahigh-contrast laser pulses,” *Physical review letters* **99**, 185002 (2007).
- ⁴⁸M. Borghesi, J. Fuchs, S. Bulanov, A. Mackinnon, P. Patel, and M. Roth, “Fast ion generation by high-intensity laser irradiation of solid targets and applications,” *Fusion science and technology* **49**, 412–439 (2006).
- ⁴⁹J. Strehlow, J. Kim, M. Bailly-Grandvaux, S. Bolaños, H. Smith, A. Haid, E. L. Alfonso, C. Aniculaesei, H. Chen, T. Ditmire, *et al.*, “A laser parameter study on enhancing proton generation from microtube foil targets,” *Scientific Reports* **12**, 10827 (2022).
- ⁵⁰A. Macchi, M. Borghesi, and M. Passoni, “Ion acceleration by superintense laser-plasma interaction,” *Reviews of Modern Physics* **85**, 751–793 (2013).
- ⁵¹M. Almassarani, S. Meng, B. Beleites, F. Ronneberger, G. G. Paulus, and A. Gopal, “Parametric study of proton acceleration from laser-thin foil interaction,” *Plasma* **4**, 670–680 (2021).
- ⁵²R. A. Simpson, G. Scott, D. Mariscal, D. Rusby, P. King, E. Grace, A. Aghedo, I. Pagano, M. Sinclair, C. Armstrong, *et al.*, “Scaling of laser-driven electron and proton acceleration as a function of laser pulse duration, energy, and intensity in the multi-picosecond regime,” *Physics of Plasmas* **28** (2021).